JGR Space Physics

RESEARCH ARTICLE
10.1029/2019JA026716

This article is a companion to Meredith et al. (2019), https://doi.org/10.1029/2019JA026715.

Key Points:
- Models of the globally averaged VLF transmitter wave power capture their long-term contribution to electron loss
- VLF transmitter waves can reduce the lifetimes of moderate-energy electrons, $E \sim 500$ keV, by an order of magnitude down to 200 days at $L \sim 1.7$
- VLF transmitter waves are unable to effectively remove multi–megaelectron volt electrons

Correspondence to:
J. P. J. Ross,
johros@bas.ac.uk

Citation:
Ross, J. P. J., Meredith, N. P., Glauert, S. A., Horne, R. B., & Clilverd, M. A. (2019). Effects of VLF transmitter waves on the inner belt and slot region. *Journal of Geophysical Research: Space Physics*, *124*. https://doi.org/10.1029/2019JA026716

Received 12 MAR 2019
Accepted 3 JUN 2019
Accepted article online 22 JUN 2019

Effects of VLF Transmitter Waves on the Inner Belt and Slot Region

J. P. J. Ross[1], N. P. Meredith[1], S. A. Glauert[1], R. B. Horne[1], and M. A. Clilverd[1]

[1]British Antarctic Survey, Natural Environment Research Council, Cambridge, UK

Abstract Signals from very low frequency (VLF) transmitters can leak from the Earth-ionosphere wave guide into the inner magnetosphere, where they propagate in the whistler mode and contribute to electron dynamics in the inner radiation belt and slot region. Observations show that the waves from each VLF transmitter are highly localized, peaking on the nightside in the vicinity of the transmitter. In this study we use ~5 years of Van Allen Probes observations to construct global statistical models of the bounce-averaged pitch angle diffusion coefficients for each individual VLF transmitter, as a function of L^*, magnetic local time (MLT), and geographic longitude. We construct a 1-D pitch angle diffusion model with implicit longitude and MLT dependence to show that VLF transmitter waves weakly scatter electrons into the drift loss cone. We find that global averages of the wave power, determined by averaging the wave power over MLT and longitude, capture the long-term dynamics of the loss process, despite the highly localized nature of the waves in space. We use our new model to assess the role of VLF transmitter waves, hiss waves, and Coulomb collisions on electron loss in the inner radiation belt and slot region. At moderate relativistic energies, E ~500 keV, waves from VLF transmitters reduce electron lifetimes by an order of magnitude or more, down to the order of 200 days near the outer edge of the inner radiation belt. However, VLF transmitter waves are ineffective at removing multi–megaelectron volt electrons from either the inner radiation belt or slot region.

1. Introduction

The life cycle of the inner electron radiation belt comprises of rapid enhancements or injections followed by long periods of decay (Rosen & Sanders, 1971). Flux enhancements for lower-energy electrons, $E \lesssim 500$ keV, generally occur a few times per year but for higher energies they are considerably less frequent (Claudepierre et al., 2017; Li et al., 2015; Looper et al., 2005). Enhancements may be by nondiffusive radial transport by increased large-scale magnetospheric electric fields (Selesnick et al., 2016; Su et al., 2016) or possibly by local wave-particle interactions (Albert et al., 2016). At very low L, atmospheric collisions are extremely effective at scattering electrons (Walt & MacDonald, 1964). The effect of atmospheric collisions rapidly decreases with increasing L (Walt & Farley, 1976), and wave-particle interactions become increasingly important. In particular, it was shown by Abel and Thorne (1998) that the combined effect of Coulomb collisions and resonant interactions with plasmaspheric hiss, lightning-generated whistlers, and anthropogenic very low frequency (VLF) transmissions, could explain the steady state, general features of the inner zone and slot region. They also showed that the modeled lifetimes were in approximate agreement with those determined from observed electron decay rates of electrons produced by the high-altitude nuclear detonation, Starfish.

Electron lifetimes in the slot region are strongly affected by resonant interactions with plasmaspheric hiss and, to a lesser extent, lightning-generated whistlers (Meredith et al., 2019). At lower L, their scattering efficiency decreases, at which point VLF transmitter waves become increasingly influential on electron populations (Abel & Thorne, 1998; Ripoll et al., 2014). Indeed, the effects of VLF transmitter waves can be directly found in DEMETER/IDP (Instrument for Particle Detection) observations of enhancements in the drift loss cone electron flux, commonly referred to as "wisps" (Gamble et al., 2008).

VLF transmitter waves used for communications with submarines have unique discrete characteristics. The transmissions are of very narrow band width 100 Hz, (Cohen et al., 2010) in the frequency range 18.3–26.7 kHz and near constant in time, other than during maintenance. A fraction of the waves leak from the Earth-ionosphere waveguide, mainly on the nightside (Helliwell, 1965; Tao et al., 2010), into the near-Earth environment, where they propagate as whistler mode plasma waves. Therefore, the signal is

geographically localized around the transmitters with a magnetic local time (MLT) dependence. In terms of L shell, they are situated at the foot of magnetic field lines in the range $L = 1.2$–3.3. Particularly prominent transmitters, by emitted power, include NWC in Exmouth, Australia (1MW), and NAA in Cutler, Maine, USA (1MW) (Clilverd et al., 2008).

Various levels of approximations have been used to calculate electron diffusion coefficients from VLF transmitter waves. Abel and Thorne (1998) used two representative frequencies to model the transmitters. In their study amplitudes were calculated using the VLF transmitter model of Inan et al. (1984). Later studies by Agapitov et al. (2014) and Ma et al. (2017) used Akebono and Van Allen Probes data, respectively, to further explore the effects of VLF transmitters. These diffusion coefficient calculations involved combining the transmitters together by MLT and longitudinally averaging. Agapitov et al. (2014) assumed a broad frequency spectrum centered at 15 kHz with a width of 7.5 kHz to encompass all of the VLF transmitters. On the other hand, Ma et al. (2017) fitted Gaussian distributions at $L = 1.5$, 2.0, and 2.5 to wave spectral power over the whole VLF transmitter frequency range. Additionally, the variation of wave parameters along magnetic field lines is rarely considered in these studies. In a more comprehensive approach, Selesnick et al. (2013) constructed geographically and MLT-dependent diffusion coefficients, in the narrow band limit with variation along the magnetic field lines considered, representing electron scattering by NWC to reproduce a wisp observation in DEMETER/IDP electron intensity (Gamble et al., 2008; Sauvaud et al., 2008). Globally averaged archetypical transmitters have generally been assumed with broad bandwidth ($\gtrsim$1 kHz) to encompass multiple transmitters. To the knowledge of the authors, there are no previous studies where geographically and MLT varying diffusion coefficients are calculated for the other transmitters. This will be the aim of this paper.

Recently, Meredith et al. (2019) studied the geographic and MLT dependence of the wave power from the 14 most powerful VLF transmitters using Van Allen Probes data. The results allow us to explore the effects of each individual VLF transmitter on the electrons in the inner belt and slot region and enable us to investigate the effects of their narrow band width, spatial structure, and MLT dependence. In particular, we address the validity of global averaging and investigate whether MLT and longitude considerations are required for these highly localized waves. The individual transmitters are then combined and their total effect determined.

In this study we assess the contribution of VLF transmitters to electron loss in the inner radiation belt and slot region using global models of VLF transmitter waves derived from Van Allen Probes observations (Meredith et al., 2019). We first describe how we calculate the appropriate quasi-linear diffusion coefficients from the wave data in section 2. In section 3 we then introduce a 1-D pitch angle diffusion model with implicit longitude and MLT dependence, which incorporates the new coefficients. In section 4, we use observations of wisps to assess the success of the model and explore the filling of the drift loss cone. In section 5 we investigate whether global averaging of the VLF transmitter wave power is appropriate for modeling trapped electron decay. In section 6 we use our new model of the VLF transmitter wave power to determine the effects of Coulomb collisions, plasmaspheric hiss, and VLF transmitters on electron lifetimes in the inner belt and slot region. Finally, we discuss our results and present our conclusions in sections 7 and 8, respectively.

2. Diffusion Coefficients

2.1. Data and Assumptions

The quasi-linear diffusion coefficients for wave-particle interactions between electrons and VLF transmitter waves are determined using the PADIE code (Glauert & Horne, 2005). The PADIE code calculates bounce-averaged diffusion coefficients in equatorial pitch angle, energy, and cross terms, for either electrons or protons interacting with any cold plasma wave mode and for a specified set of wave and plasma properties. To construct global diffusion coefficient maps, we require knowledge of the geomagnetic field, ion composition, plasma density, wave normal angle, and wave magnetic field intensity (or electric field intensity) as functions of L, MLT, longitude, and distance along magnetic field lines. For the resonance calculations we include $n = -15 \ldots, +15$ to capture contributions from higher-order resonances. This resonance range is larger than that considered by Selesnick et al. (2013), who found that only the $n = \{-1, 0, 1\}$ resonances contribute significantly. Higher-order resonances become more important at the higher energies considered here and so cannot be neglected.

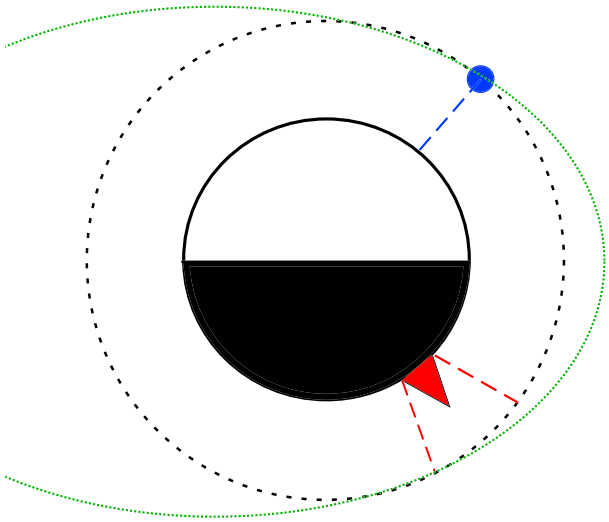

Figure 1. Schematic diagram depicting the Earth-transmitter-satellite system. The blue dot represents the satellite, and its magnetic field line connection to the Earth is shown by the blue dashed line. The red triangle depicts the transmitter, and the longitude range that it illuminates is indicated by the red dashed lines. The black dashed line represents constant L, approximately equal to the drift path of an electron, and the green dotted the satellite trajectory.

The VLF waves from a given transmitter are assumed to have a Gaussian frequency distribution of magnetic field power spectral density, centered at the VLF transmitter frequency (see Table 1 of Meredith et al., 2019) with a bandwidth of 100 Hz (as defined in Glauert & Horne, 2005). The lower and upper bounds on the wave spectrum are assumed to be ±500 Hz from the VLF transmitter frequency. The magnetic field intensities are calculated from electric field wave intensities (see section 2.2), which are determined from Van Allen Probes A satellite observations (Meredith et al., 2019). The near-equatorial wave measurements are mapped, using the Olson-Pfitzer tilt-dependent static model and the International Geomagnetic Reference Field, to their corresponding field line foot points and binned into 0.1 increments in L^*, 24 one-hour MLT segments and 120 longitude bins. If data are missing from any bin, then linear interpolation in longitude is used. For each transmitter, we select the corresponding frequency channel(s) of EMFISIS and isolate the power from the transmitter by omitting wave power that is further than 20° longitude from the transmitter by setting these values to 0. In some cases wave power from a VLF transmitter is detected in two frequency channels, in which case the above procedure is performed to both channels and then the wave power is summed. In Figure 1 we show a schematic diagram illustrating the system. We therefore have an equatorial electric field wave map, $E_{w,\mathrm{Eq}}(L^*, \mathrm{MLT}, \theta)$, for each individual transmitter, where θ is the longitude. Due to close geographic proximity and frequency, and hence over lapping wave power, we combine the VLF transmitters ICV and FTA2 into ICV+FTA2, and GVT and HWU, which occasionally operates at a frequency near that of GVT (Meredith et al., 2019), into GVT+HWU and assume a mean frequency for these combined transmitters. For the diffusion coefficient calculations and subsequent electron diffusion modeling we assume a dipole field and hence replace L^* with L.

During active conditions, chorus waves can be found at L^* as low as 3; therefore, measurements when $AE >$ 300 nT are excluded to minimize contamination of VLF transmitter wave power (Meredith et al., 2019). In fact, observations suggest that VLF transmitter power is independent of geomagnetic activity (Meredith et al., 2019; Cohen et al., 2010) and so we average the data over $AE <$ 300 nT.

The plasma frequency, f_{pe}, measured by EMFISIS High Frequency Receiver (HFR) (Meredith et al., 2019) agrees well with the statistical model by Ozhogin et al. (2012) for $L > 2.2$ but deviates to lower values from an extrapolation of the Ozhogin et al. (2012) model (calculated on the range $L = 1.6 - 4.0$) at lower L. This departure is due to sampling on EMFISIS HFR where the highest receiver frequency is 486.97 kHz and measurements of f_{pe} above this are not possible (Meredith et al., 2019). To allow us to include latitudinal variation, we adopt the Ozhogin et al. (2012) density model for our calculations. At the low L shells considered here, there is minimal MLT and longitudinal variation in f_{pe} and so we assume the average value henceforth. As

noted by Agapitov et al. (2014), the Ozhogin et al. (2012) density model agrees with the optimized density model found by Selesnick et al. (2013) to within 10% for $1.5 < L < 2.0$.

Wave normal angles of VLF transmitter waves are poorly constrained due to lack of measurements of all wave components that are needed to calculate ellipticity and hence the wave normal angle. In the first instance, are the waves ducted or nonducted? Clilverd et al. (2008) suggested that a "significant portion" of wave power at $L < 1.5$ is nonducted, while at higher L shells a considerable contribution is from interhemispherically ducted waves. Studies have suggested that ducting occurs above $L = 1.7$ (Clilverd et al., 2008; Gamble et al., 2008), while at $L > 2$ large reduction in wave power above the half gyrofrequency suggests VLF transmitter waves are largely ducted (Ma et al., 2017). A possible explanation for this was found by Clilverd and Horne (1996) who showed, using ray tracing, that higher ducting enhancement factors are need at low L shells to keep transmitter signals ducted. With this in mind, we follow Ma et al. (2017) and assume that all waves are nonducted at $L < 1.7$, 25% of electric field intensity is nonducted for $1.7 \leq L < 2.5$ and all waves are ducted at $L \geq 2.5$. The assumption that all VLF transmitter waves are ducted at $L > 2.5$ is highly simplified. In reality the picture is much more complicated; in fact, there will be a mixture of ducted and nonducted waves. Whistler mode waves can only be trapped by density enhancements at frequencies below the half gyrofrequency, while in density depletions trapping is possible up to the gyrofrequency range (Karpman & Kaufman, 1982). The half gyrofrequency cutoff will come into effect for all of the transmitters considered here between $L = 2.5$ and $L = 3.0$. Consider VLF waves from a given transmitter propagating along a field line and guided by a density enhancement. If along their trajectory the frequency exceeds the local half gyrofrequency, then the waves will no longer be fully contained and the waves may leak from the ducts. The ratio between ducted and nonducted waves will then be a function of latitude as well as L. Here we have not attempted to quantify this due to the amount of uncertainty in any calculation. Our assumption of all VLF transmitter waves being ducted at $L \geq 2.5$ over estimates the effect of VLF transmitter waves on the electron population but, as we will show in sections 6 by relaxing this assumption, this choice has little effect on our results. At each L, we then have ducted and nonducted equatorial electric field intensities, $E^{Dt}_{w,\mathrm{Eq}}$ and $E^{Nt}_{w,\mathrm{Eq}}$, respectively, for each transmitter, t.

For ducted wave propagation, we assume a Gaussian distribution in $\tan(\psi)$, where ψ is the wave normal angle, centered at $\psi_0 = 0°$ with width $\psi_w = 10°$. For nonducted waves we follow the approach of Selesnick et al. (2013), taking $\psi_0 = 30°$ at an altitude of 200 km at the magnetic foot point in the hemisphere of the transmitter and assume that the wave normal angle rotates linearly with distance along the magnetic field line until it reaches $\psi_0 = 90°$ at the other foot point. Again, $\psi_w = 10°$ is used for the width where appropriate. This prescription is in rough agreement with ray tracing simulations (Kulkarni et al., 2008; Starks et al., 2008).

2.2. Diffusion Coefficient Calculations

The calculation of quasi-linear bounce-averaged diffusion coefficients for electron interaction with VLF transmitter waves requires wave magnetic field intensities along the magnetic field line. In order to obtain this dependence, the following calculation is done individually for each transmitter. The equatorial Van Allen Probes electric field measurements for each transmitter, t, are split into ducted and nonducted components, $E^{it}_{w,\mathrm{Eq}}$, as stated above (ducted and nonducted indicated by superscript i). The ducted and nonducted equatorial wave magnetic fields, $B^{it}_{w,\mathrm{Eq}}$, and Poynting fluxes, $S^{it}_{w,\mathrm{Eq}}$, are then calculated using equations (A1)–(A7) following Albert (2012). We assume conservation of Poynting flux, for ducted and nonducted waves individually, along flux tubes in order to obtain nonequatorial values:

$$S^{it}_{w} = S^{it}_{w,\mathrm{Eq}} \frac{B}{B_{\mathrm{Eq}}}. \tag{1}$$

where B and B_{Eq} are the local and equatorial magnetic field intensities, respectively. The local wave magnetic field strength is then obtained using equation (A7).

The bounce-averaged diffusion coefficients that we calculate have five dimensions: equatorial pitch angle (α), electron energy (E), L, MLT, and θ. Storing and using a five-dimensional matrix is impractical from a computational perspective, so, to simplify, we note that the bounce-averaged diffusion coefficient from a transmitter, assuming axisymmetry other than in wave power, can be written as

$$D^{t}_{\alpha\alpha}(\alpha, E, L, \mathrm{MLT}, \theta) = \sum_{i \in \{\mathrm{ducted,\ nonducted}\}} \bar{D}^{it}_{\alpha\alpha}(\alpha, E, L)(B^{it}_{w,\mathrm{Eq}}(L, \mathrm{MLT}, \theta))^2 \tag{2}$$

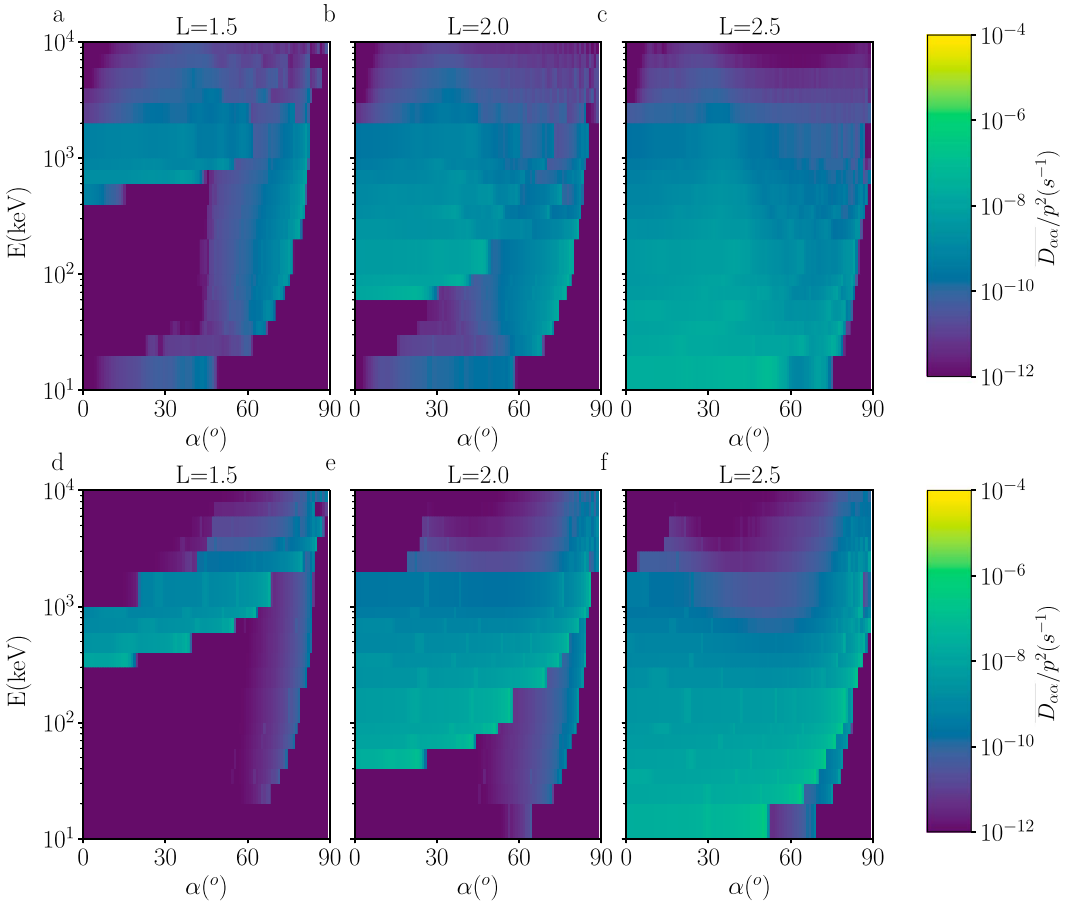

Figure 2. NWC normalized diffusion coefficients for nonducted (a–c) and ducted very low frequency transmitter waves (d–f).

where we define the normalized bounce-averaged diffusion coefficient, $\bar{D}^{it}_{\alpha\alpha}$, to be

$$\bar{D}^{it}_{\alpha\alpha} = \frac{1}{(B^{it}_{w,\mathrm{Eq}})^2} \sum_{x_i \in X} \hat{D}^{it}_{\alpha\alpha}(x_i)(B^{it}_w(x_i))^2. \tag{3}$$

X is the set of distinct field line segments, $X = \{x_1, x_2, \ldots, x_n\}$, each with a length equivalent to 5° latitude, such that when the segments are laid end to end, they cover the whole field line between its two foot points at 200 km, with no overlap. $\hat{D}^{it}_{\alpha\alpha}(x_i)$ is the bounce-averaged diffusion coefficient assuming a unity wave amplitude over the segment x_i and zero else where. The calculation of $\hat{D}^{it}_{\alpha\alpha}(x_i)$, using PADIE (Glauert & Horne, 2005), assumes that there is minimal change in density within a segment; these values are evaluated at the center of the segment. The density is allowed to vary between segments, retaining the latitudinal dependence. The $(B^{it}_w(x_i))^2$ factor accounts for the variation in wave power along the magnetic field. Note that $\bar{D}^{it}_{\alpha\alpha}$ has no longitude and MLT dependence as $B^{it}_w/B^{it}_{w,\mathrm{Eq}}$ and $\hat{D}^{it}_{\alpha\alpha}$ are independent of MLT and longitude in an axisymmetric system.

$D^t_{\alpha\alpha}$ is then calculated, in equation (2), by scaling $\bar{D}^{it}_{\alpha\alpha}$ by the local equatorial magnetic field intensity corresponding to that transmitter and summing over ducted and nonducted wave types. Note that $D^t_{\alpha\alpha}$ is now a function of L, MLT and longitude. Finally, we can sum over all the transmitters to obtain combined VLF transmitter diffusion coefficients

$$D^T_{\alpha\alpha}(\alpha, E, L, \mathrm{MLT}, \theta) = \sum_{t \in T} D^t_{\alpha\alpha}(\alpha, E, L, \mathrm{MLT}, \theta). \tag{4}$$

For comparison we calculate MLT and longitude averaged diffusion coefficients for each individual transmitter, $\langle D^t_{\alpha\alpha} \rangle_{\mathrm{MLT},\theta}$ and sum over all transmitters to obtain $\langle D_{\alpha\alpha} \rangle^T_{\mathrm{MLT},\theta} = \sum_{t \in T} \langle D^t_{\alpha\alpha} \rangle_{\mathrm{MLT},\theta}$, the total MLT

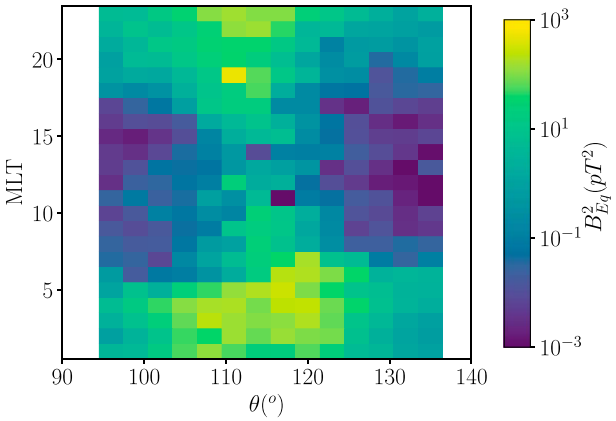

Figure 3. Cross section of equatorial magnetic field intensity from NWC at $L = 1.5$ showing longitudinal and magnetic local time (MLT) dependence. Note the reduced longitude range.

and longitudinally averaged diffusion coefficients. Henceforth, for brevity, we refer to MLT and longitude averaging as global averaging.

2.3. Normalized Diffusion Coefficients

To understand the general features of the diffusion coefficients, we first consider the form of the diffusion coefficients for unit wave power in the equatorial region, $\bar{D}^{it}_{\alpha\alpha}$. In Figure 2 we plot $\bar{D}^{i}_{\alpha\alpha}$ resulting from a unit power (pT^2) transmitter emitting at 19.8 kHz situated in Southern Hemisphere for three choices of L for nonducted (a)–(c) and ducted waves (d)–(f). At any given L, we identify, by limiting the resonance range, that the band of diffusion, between 60° and 90° equatorial pitch angle is from Landau resonance interactions. The remaining bands of diffusion are a result of cyclotron resonances; these extend down to $\alpha = 0°$ for a range of energies. The minimum energy of the cyclotron resonance decreases with increasing L due to the decreasing cyclotron frequency (Ma et al., 2017; Mourenas et al., 2012). It is worth noting that below this minimum energy, without any additional diffusion mechanism, there is a band of electrons that will not be scattered into the loss cone by VLF transmitter waves, nor will they be diffused from high to low equatorial pitch angles.

The ducted and nonducted diffusion coefficients are generally similar; however, there are subtle differences. The nonducted waves give stronger diffusion from Landau resonances than ducted waves as Landau resonances are not permitted for wave that are strictly parallel propagating. These stronger interactions allow

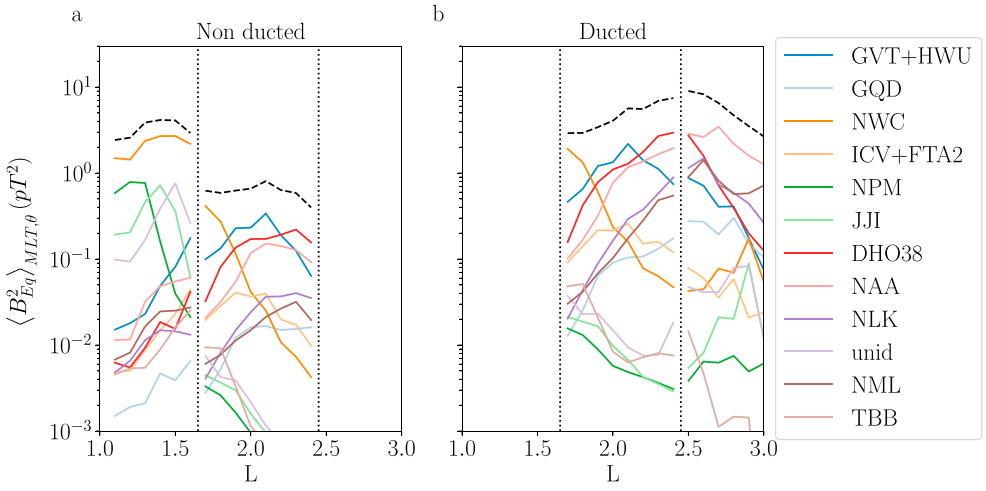

Figure 4. Magnetic local time and longitudinally averaged equatorial magnetic field intensities for very low frequency (a) ducted and (b) nonducted waves from the transmitters considered. The vertical dashed lines indicate the L shells where the ducted to nonducted ratio changes. Below $L = 1.7$ all waves are ducted, for $1.7 \leq L < 2.5$ the electric field intensity is split 75%/25% in favor of ducted waves, and for $L \geq 2.5$ the waves are all ducted.

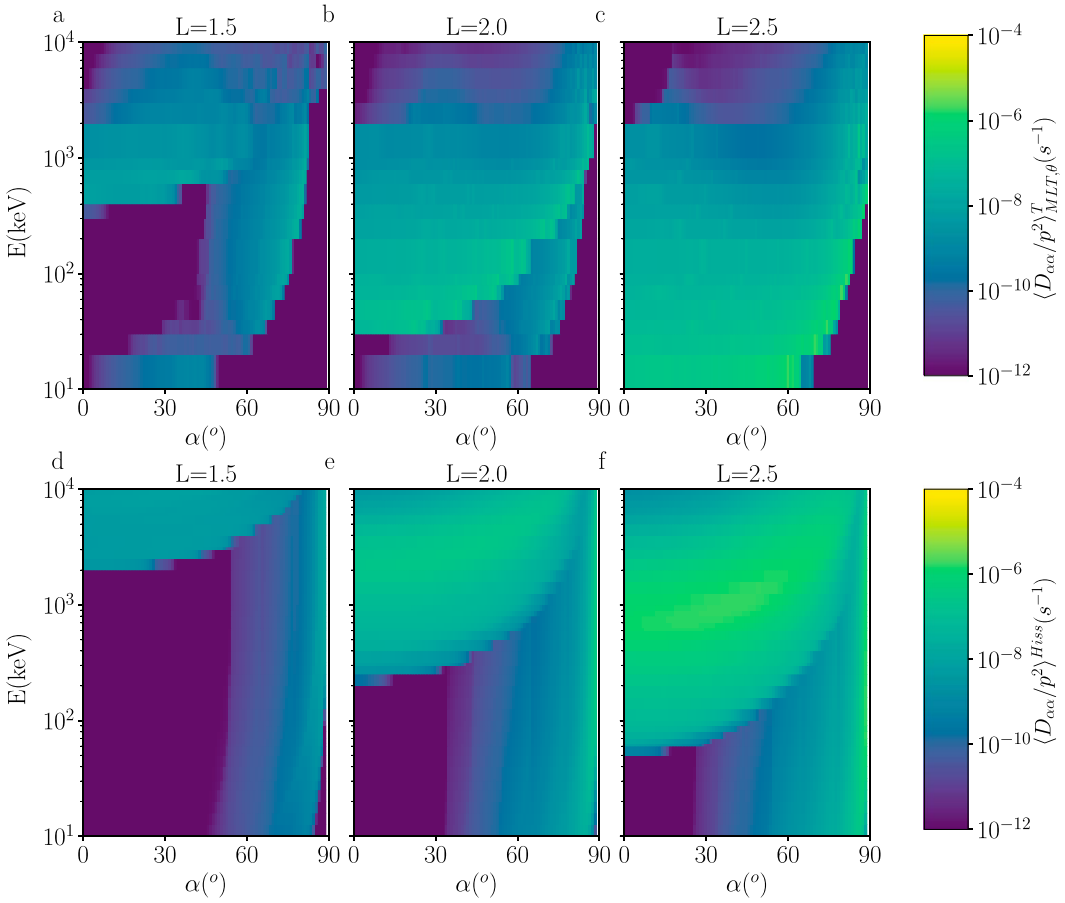

Figure 5. Magnetic local time (MLT) and longitudinally averaged diffusion coefficients for all transmitters, $\langle D_{\alpha\alpha}/p^2\rangle^T_{\mathrm{MLT},\theta}$ (a–c). For comparison hiss diffusion coefficients are shown at $0 \leq Kp < 1$ (d–f).

faster scattering of high equatorial pitch angle electrons. At low L, $L \sim 1.5$–2, nonducted waves have more extensive resonance coverages of (α, E) phase space, especially at $E \gtrsim 1$ MeV. Additionally, the minimum energy of the cyclotron resonance is lower for the ducted case allowing diffusion of lower-energy electrons into the loss cone. At the lowest energies considered, ~10 keV, nonducted waves, unlike their ducted counterparts, are able to scatter electrons that are close to the loss cone.

2.4. Spatial and MLT Dependence

The normalized diffusion coefficients, shown in the previous section, are scaled by the equatorial magnetic field intensity, $(B^i_{w,Eq}(L, \mathrm{MLT}, \theta))^2$, to obtain our global, L, MLT, and θ dependent, diffusion coefficient map for each transmitter. $(B^i_{w,\mathrm{Eq}}(L, \mathrm{MLT}, \theta))^2$, determined from Van Allen Probes observations, has important structure that we illustrate here.

In Figure 3 we show the MLT and longitudinal variation of VLF transmitter wave power from NWC at $L = 1.5$. Intensities are strongest on the nightside and localized around the transmitter's longitude. For this particular slice, the intensity reaches ~300 pT^2 in comparison to an average value of ~2 pT^2. In fact, for all transmitters, the bulk of VLF transmitter wave power is when the VLF transmitter is located on the nightside and in the vicinity of the transmitter. We therefore expect their effect on electrons to be restricted correspondingly.

VLF transmitter waves in the Earth-ionosphere wave guide can propagate away from the transmitter before leaking through the ionosphere into the inner magnetosphere. Therefore, wave power from a single transmitter is spread over a region around the source, which corresponds to a range of L values. The L dependence of the MLT and longitudinally averaged equatorial magnetic field intensities of the transmitters are shown in Figure 4. The majority of VLF transmitter wave power in the inner electron belt at $L < 1.7$ is from NWC, with smaller contributions from NPM, JJI, and unid25. At larger L, $L > 1.7$, the majority of the wave power

is from DHO38, NAA, and GVT+HWU. From this we infer that NWC will have the strongest effect on the electron population at $L < 1.7$, with DHO38, NAA, and GVT+HWU dominating the VLF transmitter contribution at larger L.

2.5. Averaged Diffusion Coefficients

The MLT- and longitude-dependent diffusion coefficients that have been constructed in the previous two sections ensure that the variation in VLF transmitter wave power can be effectively represented in modeling the radiation belts. In particular, the power maxima, and hence diffusion coefficient maxima, on the nightside over the transmitters are captured. However, the bulk of global radiation belt models do not take these variations into account and simply average over MLT and longitude. To test this assumption, we construct globally averaged diffusion coefficients $\langle D_{\alpha\alpha}\rangle^{T}_{\mathrm{MLT},\theta}$. Also, these diffusion coefficients can be compared to the diffusion coefficients of Ma et al. (2017), who combined the narrow band width transmitters (100 Hz) into a two broad band signals (full widths of 1 kHz at $L = 1.5$ and 1.8 kHz at $L = 2$ and 2.5) and averaged over MLT and longitude. Additionally, unlike Ma et al. (2017), we retain the latitudinal dependence along field lines of density, wave intensity, and wave normal angle.

In Figure 5 we show the globally averaged diffusion coefficient, summed over the individual transmitters, $\langle D_{\alpha\alpha}\rangle^{T}_{\mathrm{MLT},\theta}$. We showed in Figure 4 that NWC has the strongest wave power at $L = 1.5$ of approximately 2 pT^2. The frequency of the modeled transmitter in Figure 2 corresponds to NWC; therefore, Figure 5a closely resembles Figure 2a given that we are assuming all waves are nonducted at this location. At $L = 2$, there are more contributors to the total power: DH038, NAA, and GVT+HWU participate through ducted and nonducted waves. This leads to combined diffusion coefficients that have broader and smoother coverage in α, E than the individual transmitters. At larger L, at $L = 2.5$ where we assume all waves are ducted, there are five major contributors to electron scattering: DHO38, NAA, GVT+HWU, NLK, and NML. Figure 5c closely resembles Figure 2f indicating that the diffusion coefficients are relatively insensitive to frequency over the transmitter frequency range, 18.3–25.2 kHz. The pitch angle diffusion coefficients shown in Figures 5a–5c agree approximately with those calculated by Ma et al. (2017, Figure 3, top panel), both in magnitude and shape. For instance, at $L = 2.5$, E ~200 keV and $\alpha \sim 85°$, both sets of diffusion coefficients calculations obtain $D_{\alpha\alpha} \approx 10^{-6}(\mathrm{s}^{-1})$.

Of course, VLF transmitter waves do not act alone in electron pitch angle scattering. Hiss waves are also present and are particularly effective at electron diffusion in the slot region, Figures 5d–5f. Here and henceforth, we assume hiss covers the frequency range 0.1–5 kHz and includes magnetospherically reflected lightning-generated whistlers a frequencies above 2 kHz (Meredith et al., 2006). However, as with VLF transmitter waves, hiss wave-driven electron pitch angle diffusion has a minimum between the Landau resonance and the cyclotron resonances at around ~75°. If hiss were acting alone, then this would hinder electron diffusion from high pitch angles, leading to top hat equatorial pitch angled distributions and longer decay times. There is an offset in α between the VLF transmitter diffusion minimum and that of hiss, and so combining partially fills the hiss diffusion minimum, speeding up diffusion. Hiss waves are of lower frequency than VLF transmitter waves and so the minimum energy of cyclotron resonances for hiss is greater than for VLF transmitter waves. For instance, at $L = 1.5$, hiss waves do not diffuse $E \lesssim 1$ MeV electrons at $\alpha < 50°$ and so are unable to scatter these electrons into the loss cone. In comparison, VLF transmitter waves are able to do so for energies down to 300 keV: It is VLF transmitter waves' electron scattering at low L, low E, and low α that leads to observable flux enhancements in the drift loss cone; see section 4.

In addition to the pitch angle diffusion coefficients shown here, we also calculate the corresponding energy and cross-term diffusion coefficients. These are typically an order of magnitude lower in amplitude in comparison to the pitch angle term and hence are of secondary importance.

3. One-Dimensional Pitch Angle Diffusion Model

Selesnick (2012) and Selesnick et al. (2013) constructed a set of stochastic differential equations with MLT and longitude variation to model the inner belt. Here we take a simpler approach and reduce the system to a 1-D pitch angle diffusion equation with MLT and longitude changes included implicitly through the time dimension. Our aim is to examine the time scales for loss in the inner belt, especially focusing on the significance of VLF transmitter waves and the effect of their inhomogeneous power in the radiation belts.

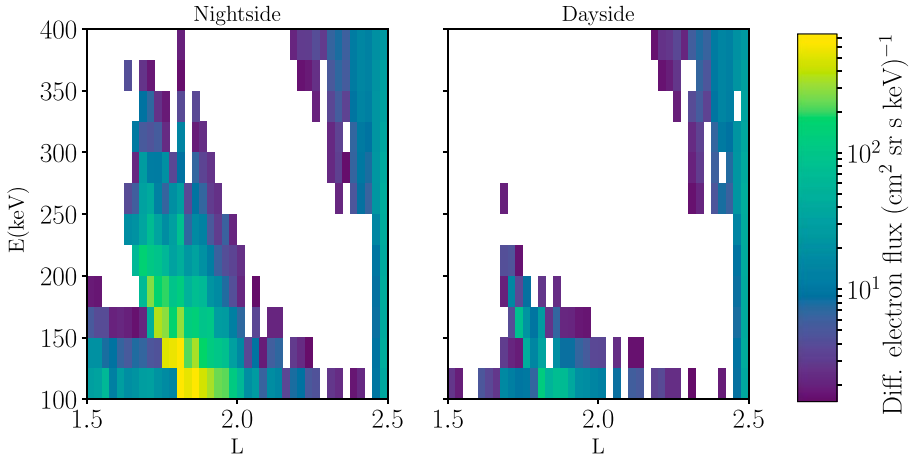

Figure 6. Drift loss cone electron flux near 250° (west of the South Atlantic Anomaly) with only NWC very low frequency transmitter waves, hiss waves, and Coulomb collisions included in the 1-D pitch angle model. Each cell is a separate model run.

In this paradigm we "follow" a band of electrons around the Earth and keep track of the MLT of the transmitters. For this we neglect the variation in drift rate around the Earth with pitch angle and instead we adopt a representative rate corresponding to a equatorial pitch angle near the loss cone (30°). The electrons experience pitch angle scattering from VLF transmitter waves and hiss waves, Coulomb collisions, and atmospheric losses based on their longitude. The pitch angle scattering by the VLF transmitter waves is localized around transmitters and is dependent on the MLT of the transmitter, which as Figure 3 shows, varies considerably based on whether the transmitter is on the nightside or not. The bounce-averaged Coulomb scattering diffusion coefficients are calculated following Abel and Thorne (1998). The neutral densities are taken from the model NRLMSISE-00 (Picone et al., 2002) and the plasma densities from the GCPM (Gallagher & Craven, 2000). The calculation is performed assuming fixed longitude (0°), universal time (UT, 12:00), date (21 June 1995), *Ap* (7, roughly corresponding to $Kp = 2$), and $F_{10.7}$ (150). To replicate longitudinal variation, these diffusion coefficients are then shifted in equatorial pitch angle by the difference between the local loss cone pitch angle and the loss cone pitch angle at the location at which the diffusion coefficients were initially calculated. Ideally, the Coulomb scattering diffusion coefficients would be calculated over the range of longitude and UT but this is beyond the scope of this work. Meredith et al. (2018) is used for the hiss diffusion coefficients, where chorus waves are excluded by use of an activity-dependent plasmapause model (Horne et al., 2013).

The distribution function, f, at each pitch angle can be evolved by solving

$$\frac{\partial f}{\partial t} = \frac{1}{T \sin 2\alpha}\left(\frac{\partial}{\partial \alpha}\left[D_{\alpha\alpha}(t) T \sin 2\alpha \frac{\partial f}{\partial \alpha}\right]\right) - \frac{f}{\tau_L(\theta(t))} \tag{5}$$

(Albert & Shprits, 2009; Lyons et al., 1972), where $D_{\alpha\alpha}$ is the sum of hiss wave-particle interactions, Coulomb scattering, and transmitter wave-particle interactions, $D^T_{\alpha\alpha}$. In addition to the longitude of the electrons, the MLT sector of the transmitters are recorded. $D^T_{\alpha\alpha}$ is then chosen corresponding to the MLT of the transmitters and the longitude of the electrons. For example, the VLF wave power from NWC, and hence the diffusion coefficient, experienced by electrons drifting over the transmitter that is in a given MLT sector, will follow a horizontal line across Figure 3. For the drift velocity, v_d, we use the approximation formula from Spjeldvik and Rothwell (1985):

$$v_d = 2\pi \frac{L\gamma(v/c)^2(1 + 0.42 \sin \alpha)}{1.43 K_t} \tag{6}$$

where $K_t = 1.0308 \times 10^4$ s. For comparison, we also use the MLT and longitude averaged version, $\langle D_{\alpha\alpha} \rangle^T_{\mathrm{MLT},\theta}$, as defined in section 2.1. For the work presented in this paper, we assume quiet time conditions ($0 \leq Kp < 1$) for our hiss diffusion matrix to represent undisturbed decay of the inner regions, calculated using Meredith

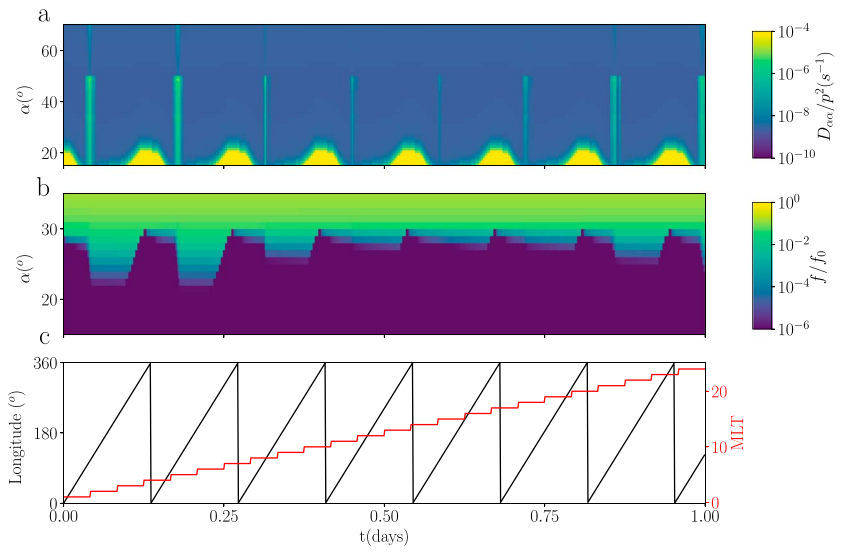

Figure 7. (a) Total diffusion coefficient from Coulomb collision, hiss, and NWC very low frequency transmitter waves as a function of time at $L = 1.75$ for a 200-keV electron. (b) The pitch angle distribution near the loss cone is shown during the same period in (b). (c) The longitude of the electron population and the magnetic local time (MLT) sector of the transmitter.

et al. (2018). $T(\alpha)$ approximates the mirror latitude dependence of the bounce period. The loss rate is given by

$$\tau_L = \begin{cases} 0.25\tau_b, & \text{for } \alpha < \alpha_{LC}(\theta(t)) \\ \infty, & \text{otherwise} \end{cases}$$

where τ_b is the bounce period. The equation is solved using an implicit time stepping method. Zero-gradient ($\partial f/\partial\alpha = 0$) boundary conditions are used at $\alpha = 0°$ and 90° assuming that collisions deep inside the loss cone are sufficiently high to make the distribution isotropic.

In this model, radial diffusion, energy diffusion, cross terms, and azimuthal variation in drift rate are neglected, but each of these factors is generally less important than pitch angle scattering in the inner regions. Radial diffusion is over long times during quiet periods at low L (Brautigam & Albert, 2000). Rapid radial transport does occur during injection events in geomagnetically disturbed times, but here we are interested in the decay of existing particles. For the values of f_{pe}/f_{ce} found at $1.2 < L < 3$, energy diffusion is usually much smaller than for pitch angle diffusion (Lyons et al., 1972). The drift period depends weakly on pitch angle with a factor $\sqrt{2}$ change over the 90° range; therefore, this assumption will have minimal effect. The simplicity and reduced nature of our setup allows for clear illustration and evaluation of the effects of VLF transmitters on electron pitch angle distributions. These results can then be used as an aid for interpreting more physical, complex models as well as assessing the validity of assumptions upon which they rely.

4. Model Validation

Wisps are enhancements in drift loss cone electron fluxes with an energy and L dependence and are observed by IDP on DEMETER at an altitude of 800 km (Gamble et al., 2008; Sauvaud et al., 2008). The enhancements are found at $1.6 \lesssim L \lesssim 2$ and $100 \lesssim E \lesssim 375$ keV. Longitudinally, they are observed eastward of NWC (114°E) but westward of the South Atlantic Anomaly (SAA, at ~300°E). They are a result of wave-particle interactions with VLF transmitter waves from NWC, scattering electrons into the drift loss cone, before they are lost to the atmosphere on the western side of the SAA. These observations provide an opportunity for us to asses our VLF transmitter electron diffusion model. Additionally, we can examine how strongly electrons are scattered into the drift loss cone. More precisely, is the wave power sufficient for "strong diffusion" to occur over NWC when it is on the nightside? Under strong diffusion, electrons are scattered across the loss cone in less than a quarter-bounce period, leading to an isotropic loss cone flux (Kennel, 1969). In this case,

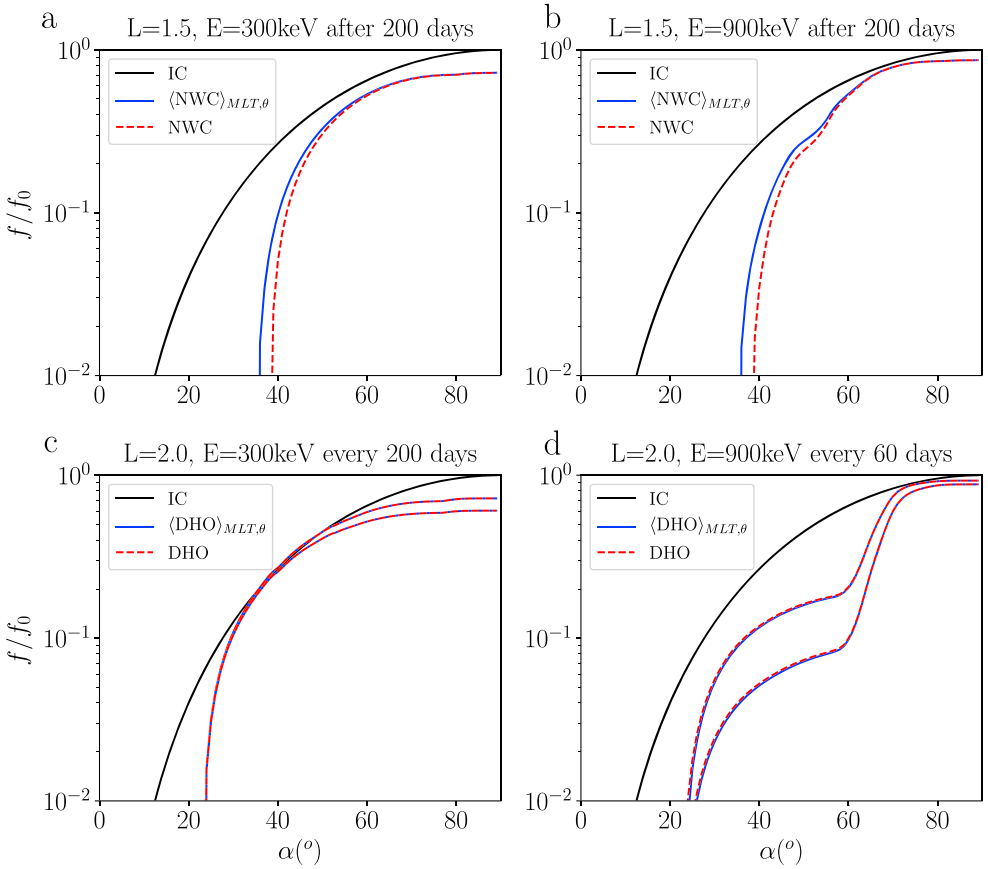

Figure 8. Instances of electron distribution at (a and b) $L = 1.5$ and (c and d) $L = 2.0$ for $E = 300$ and $E = 900$ keV. The blue curve is from the magnetic local time (MLT) and longitudinally averaged model and the red dashed are from the full prescription. For the two L shells, $L = 1.5$ and 2.0, NWC and DHO38 are the only transmitters included, respectively. Initial condition is shown by the black curve.

the rate of particle precipitation is independent of the magnitude of the diffusion coefficient (Summers & Thorne, 2003).

4.1. Method

In order to investigate whether our model is able to produce drift loss cone flux enhancements, we investigate the combined effects of the transmitter NWC along with hiss waves and Coulomb scattering. Exact replication of individual wisps is outside the scope of this work; for instance, appropriate initial conditions (equatorial pitch angle distributions, spectra, and L dependence) must be determined, as well as an event specific density profile. Instead, we take a statistical approach and take average values as our initial conditions. We assume an initial pitch angle distribution of $f = f_0(E, L)\sin^3(\alpha)$. The equatorially mirroring electron flux is calculated from the empirical electron model environment AE-8 (Vette, 1991), $f_0(E, L)$, and the exponent is chosen considering Shi et al. (2016) who performed a survey on electron pitch angle distributions using Van Allen Probes MagEIS measurements.

After running the simulations for 1 day, we calculate the average electron flux over the next day in the longitude range 240–260°E, for nightside and dayside NWC separately. The results are shown in Figure 6. When NWC is on the nightside, enhanced electron fluxes are observed between $1.6 \lesssim L \lesssim 2$ and $100 \lesssim E \lesssim 350$ keV. The energy at which the flux enhancement occurs decreases with increasing L. The shape and magnitude of the model wisp are broadly consistent with the IDP observations (Gamble et al., 2008). However, the width of the computed wisp is slightly greater than what is typically observed. This difference maybe due to our initial condition or may indicate that our diffusion coefficients are over estimating the diffusion above the minimum energy of cyclotron resonance. It is worth pointing out that the equatorial wave power from NWC (Figure 4) peaks at a lower L shell, $L \sim 1.5$, than the minimum energy of the wisp.

This is because the diffusion rate corresponding to the $n = -1$ cyclotron resonance decreases as L decreases, as shown in Figure 2. The results are substantially different when NWC is on the dayside, and we find only very low amplitude flux enhancement due to the low transmitter wave intensity.

In the slot region at $L \gtrsim 2.4$, lightning-generated whistlers and plasmaspheric hiss are effective at pitch angle scattering electrons at energies as low as a few tens of kiloelectron volts (Figure 9 and Meredith et al., 2007). Consequently, electrons are diffused rapidly into the drift loss cone over a broad energy range, independent of VLF transmitter operation (Gamble et al., 2008). Therefore, above $L \sim 2.4$ it is difficult to observe the effects of any transmitter on drift loss cone electron flux.

4.2. Drift Loss Cone Filling

We can use our model to study the process of flux enhancement and address the question of strong diffusion in the loss cone. In Figure 7 we show the time evolution of $E = 200$ keV electrons at $L = 1.75$ in our 1-D model. Electrons drifting around the Earth experience pitch angle scattering that is modulated periodically on two time scales: the drift time scale and the Earth's rotation period. The variation in the resulting diffusion coefficients are shown in Figure 7a. The large-amplitude diffusion coefficients near the loss cone, varying periodically on the drift period, are from Coulomb collisions. Superimposed onto this cyclic behavior are the scattering enhancements by VLF transmitter waves from NWC when the electrons are on field lines with footpoints near to NWC (114°E). In turn, these intervals of intense scattering are affected by the MLT of the transmitter and strongest on the nightside, Figure 7c. The resulting pitch angle distributions close to the loss cone are shown in Figure 7b. When the electrons pass over NWC while on the nightside, electrons are scattered into the drift loss cone by the enhanced VLF transmitter wave power. However, even directly over NWC, electron scattering into the drift loss cone is weak and is unable to fill the bounce loss cone; hence, the VLF transmitter waves are insufficiently intense to lead to strong diffusion. The electrons then drift eastward until they encounter the SAA (∼300°E) where those inside the drift loss cone are lost to the atmosphere.

5. Validity of Globally Averaging

In global radiation belt models, the whole electron distribution is important and small variations in flux near the loss cone need not be captured, unless they have an impact on the larger population. As we have shown, the scattering from VLF transmitter waves is highly geographically localized and largely restricted to when the source transmitter is on the nightside. This inhomogeneity then opens the question of whether MLT and longitude averaging, and summing over the transmitters, is appropriate for global radiation belt models or whether a full prescription is necessary. In particular, is the decay of the electron distribution affected by global averaging? To answer this question, we consider one transmitter in isolation at two representative L. For $L = 1.5$ and 2.0 we take NWC and DHO38, respectively, given that they are among the strongest contributors at these locations. The same initial condition is taken as in section 4. Both globally averaged, and MLT and longitudinally dependent coefficients are adopted and compared. In the globally average case, we also adopt a constant bounce loss cone equal to the drift loss cone, to remove all MLT and longitude dependence.

The results of our comparison runs are shown in Figure 8. In all four situations shown, and also all other tested configurations, there is good agreement between the two models. At $L = 1.5$, for both the 300 and 900keV electrons shown in Figures 8a and 8b, despite significant losses close to the loss cone the decay of large pitch angle electrons after 100 days is minimal, indicating very long decay time scales. During the drift period of the electrons and the rotation period of the Earth, that is, the time scales upon which the VLF transmitter wave power changes as experienced by the electrons, the pitch angle distribution does not change significantly, and hence, the diffusion of pitch angle distribution is well represented by the average diffusion coefficients. At $L = 2.0$, Figures 8c and 8d, the decay time scales are shorter but still the globally averaged model suffices and captures the profiles well. These results are general for all VLF transmitters and are not limited to the cases shown here. The validity of averaging is a result of pitch angle diffusion acting on a longer time scale than the electron drift period. The results would likely differ if more rapid local scattering occurred and the bounce loss cone was substantially filled locally.

6. Electron Lifetimes

As we have seen in the section 4, wave-particle interactions and Coulomb collisions scatter electrons into the loss cone. In this situation, diffusion coefficients close to the loss cone largely determine the electron

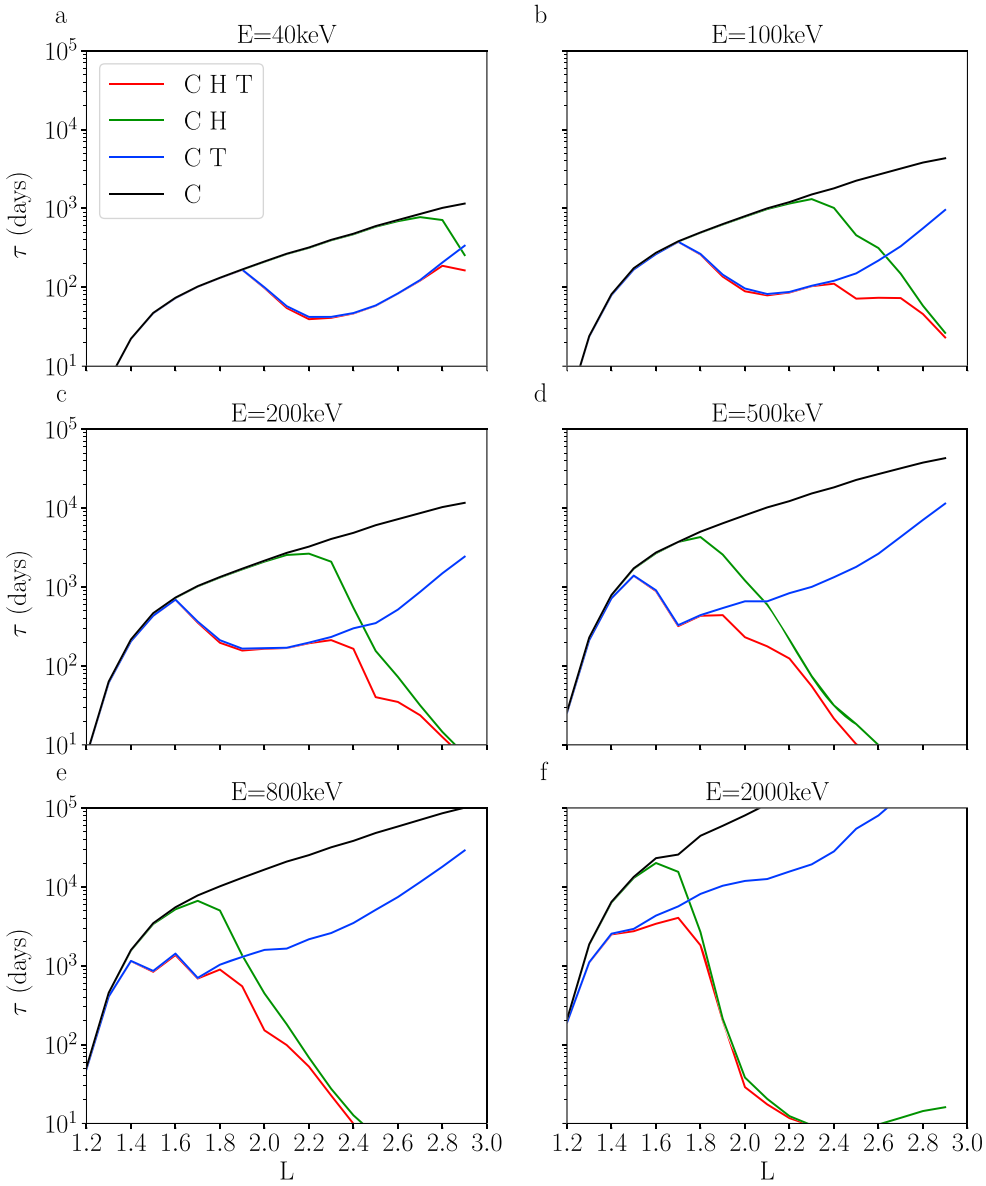

Figure 9. (a–f) Electron decay time scales from the 1-D model with magnetic local time and longitude averaging. The lines correspond to: black - Coulomb collisions; green - hiss and Coulomb collisions; blue - very low frequency transmitters and Coulomb collisions; red - very low frequency transmitters, hiss, and Coulomb collisions.

fluxes and losses, with orders of magnitude variations occurring on drift time scales. However, electrons at low pitch angles only comprise a small proportion of the total population. The behavior of high pitch angle electrons can, in some circumstances, be largely detached from the short time scale changes at low pitch angles (Albert, 2008). An extreme example would be when there is zero diffusion at some intermediate pitch angle but rapid diffusion close to the loss cone: Electrons at higher pitch angles would then remain indefinitely while those at low pitch angles would decay. Physically, such an extreme case will not occur but deep diffusion minima do exist, such as for $\alpha \sim 75°$, $E = 1$ MeV electrons at $L = 2.0$ scattered by hiss waves; see Figure 5e. Therefore, to determine representative electron lifetimes, it is necessary to consider the changes to the whole electron distribution.

In the previous section we showed that electron diffusion models using globally averaged VLF transmitter diffusion coefficients agree well with models including MLT and longitude variation. With this in mind, we proceed using the globally averaged model and adopt $\langle D_{\alpha\alpha} \rangle^{T}_{\mathrm{MLT},\theta}$ from now on. Solutions to 1-D pitch angle diffusion equations with time constant diffusion coefficients and no source terms typically reach a steadily

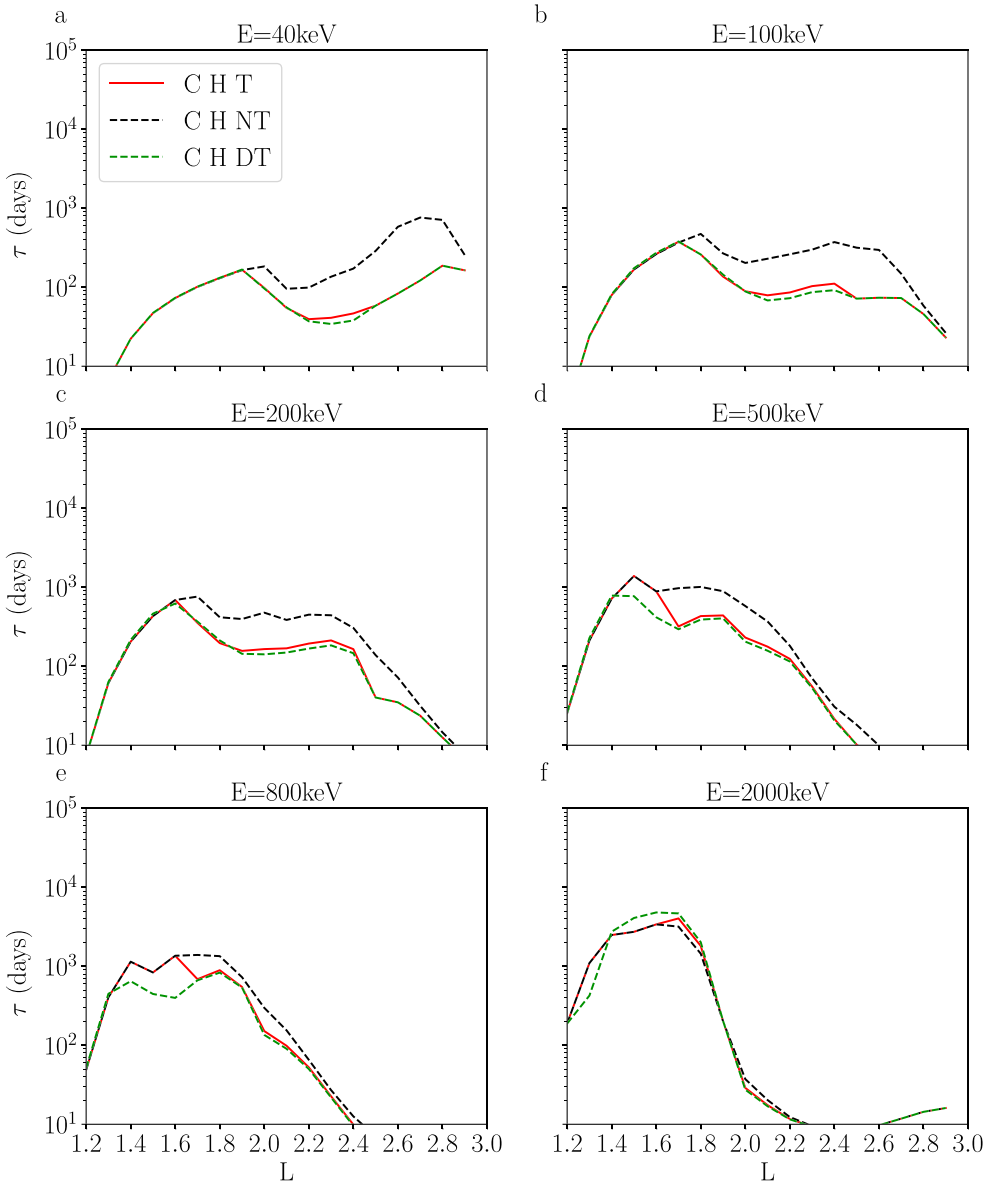

Figure 10. Electron decay time scales from the 1-D model with magnetic local time and longitude averaging. The lines correspond to: red solid - transmitters, hiss, and Coulomb collisions; black dashed line - nonducted transmitters, hiss, and Coulomb collisions; green dashed line - ducted transmitters, hiss, and Coulomb collisions.

decaying pitch angle distribution where the shape is preserved but the flux decays (Spjeldvik & Thorne, 1975). Such time scales give an indication of the time periods upon which the whole population decays subject to only pitch angle scattering. We define the electron lifetime, τ to be $f(t) = f'(\alpha)\exp(-(t-t')/\tau)$ where is f' is the distribution at an arbitrary time, t', once the profile has reached its steady shape. In order to determine which processes are important, lifetimes are calculated with selected combinations of Coulomb collisions, hiss waves, and VLF transmitters. The resulting electron lifetimes are plotted in Figure 9.

At low energy, $E \sim 40$ keV, Figure 9a, Coulomb collisions completely determine electron lifetimes at $L \lesssim 1.9$. Between $1.9 \lesssim L \lesssim 2.8$, VLF transmitter waves contribute significantly to electron scattering and are able to reduce 40 keV electron lifetimes to as low as 30 days at $L = 2.3$. Only at $L \gtrsim 2.8$ does hiss become important. The order in which the different contributors to pitch angle scattering dominate the lifetimes consistently follows this trend for $E \lesssim 800$ keV, while the L shells where the transitions between the dominant contributions occur changes. In particular, the range in L for which VLF transmitter waves are important shifts to lower values as energy is increased. For instance, at 500 keV (Figure 9d), Coulomb collisions dominate

the lifetimes at $L \lesssim 1.5$, while VLF transmitter waves strongly impact lifetimes in the range $1.6 \lesssim L \lesssim 2.2$, beyond which point hiss waves largely determine electron lifetimes, reducing lifetimes down to ~10 days at $L = 2.5$. Importantly, for ~500 keV electrons, including the contribution from VLF transmitters reduces their lifetimes by over an order of magnitude between $1.7 \lesssim L \lesssim 1.9$. At higher energies, the contributions from transmitters become weaker. At $E = 800$ keV, (Figure 9e), VLF transmitter waves reduce lifetimes by typically less than an order of magnitude, with $\tau \sim 10^3$ days at $1.4 \lesssim L \lesssim 1.8$. At $L \gtrsim 1.9$, hiss waves over take the contributions from VLF transmitter waves and reduce lifetimes to below 100 days by $L \sim 2.2$. In fact, hiss waves determine the electron lifetimes for $E \gtrsim 800$ keV electrons outside of $L \sim 1.8$.

Electrons with energies above 500 keV at L shells below $L = 1.6$ consistently have exceptionally long lifetimes with $\tau \gtrsim 10^3$ days, even with VLF transmitter waves included. Such time scales are less than those reported by Ma et al. (2017), who omitted Coulomb collisions, but considerably longer than Abel and Thorne (1998) by up to an order of magnitude at ~800 keV due to our lower VLF wave power. Our results suggest that VLF transmitters are ineffective at removing multi–megaelectron volt electrons from the inner belt and slot region during quiet time conditions except on very long time scales.

Given the uncertainty around the proportion of ducted and nonducted VLF transmitter wave power, we consider the two extreme cases: fully nonducted and fully ducted. In Figure 10 we plot electron lifetimes assuming that all of the waves are ducted (green dashed) and nonducted (black dashed). For $E \lesssim 800$ keV, nonducted waves are less effective at electron scattering than ducted waves. For $E = 40$ keV, time scales for nonducted waves can be over an order of magnitude longer at $L = 2.5$. However, in general, the difference is considerably less: τ is between 1 and 4 times longer for nonducted waves than ducted. At 2 MeV, transmitters are ineffective at pitch angle scattering for both the ducted and nonducted cases and their associated electron lifetimes are comparable. In the majority of situations, τ in our central (ducted and nonducted) case lies between the two extreme cases but can on occasion be marginally shorter.

7. Discussion

VLF transmitter signals are localized in space and maximize when the transmitter is on the nightside. This raises the question of whether longitude and MLT need to be taken into account for Fokker-Planck-based diffusion models or whether averaging over these dimensions is justified. We find that 1-D pitch angle diffusion models with implicit longitudinal and MLT variation are well represented by MLT and longitudinally averaged models: Electron lifetimes are sufficiently long compared to the variation time scale of VLF wave power experienced by electrons as they drift around the Earth. These results confirm that averaging in MLT and longitude is appropriate for VLF transmitter wave considerations outside of the loss cone in global 3-D electron radiation belt models (pitch angle, energy, and L shell).

VLF transmitter waves can be effective at reducing electron lifetimes although the L shell and energy dependence is complex. Electron lifetimes can be reduced by over an order of magnitude for $E \lesssim 800$ keV. At $E = 800$ keV this occurs at $L \sim 1.8$, while for $E = 100$ keV the maximum reduction is at larger L, $L \sim 2.2$. VLF transmitters have a considerably smaller effect on higher-energy electrons. Even including VLF transmitter waves, lifetimes for 2 MeV electrons are over 10^3 days at $L \lesssim 1.8$. In particular, there is no indication that transmitter waves lead to rapid removal of high-energy electrons in the inner region. For example, lifetimes for $\gtrsim 800$ keV electrons is a year or more at $L > 2.5$ (blue lines in Figures 9e and 9f). It is therefore difficult to see from our work how VLF transmitter signals can be responsible for the so-called impenetrable barrier of multi–megaelectron volt electrons as has been suggested previously (Foster et al., 2016).

The electron lifetimes can be understood by considering the diffusion coefficients in Figure 5 and noting that electron lifetimes can be estimated by $\max_\alpha\{1/(D_{\alpha\alpha}\tan(\alpha))\} = \tau_A \sim \tau$ (Albert & Shprits, 2009). At $L = 1.5$, Figures 5a and 5d, Coulomb collisions are the only mechanism scattering electron in the parameter space given by $20 \lesssim E \lesssim 500$ keV and $\alpha \lesssim 45°$, and hence, they determine the minimum of $D_{\alpha\alpha}\tan(\alpha)$ and the lifetimes. At higher energies, VLF transmitter waves are able to resonate with the electrons at $\alpha \lesssim 45°$, scattering them and hence increasing the minima in $D_{\alpha\alpha}\tan(\alpha)$ and decreasing τ. At $L = 2$, Figures 5b and 5e, VLF transmitter waves are able to scatter electrons consistently in the range $30 \lesssim E \lesssim$2,000 keV and $\alpha \lesssim 75°$. Hiss waves on the other hand cannot; their scattering is strong but limited to energies above 200 keV at low pitch angles (corresponding to cyclotron resonances) and to high pitch angles over all considered energies (corresponding to Landau resonances). Importantly, there is a deep minima in $D_{\alpha\alpha}$ between these two regions. VLF transmitter waves partially fill this gap at energies below ≲1 MeV and consequently reduce

τ. At $L = 2.5$, Figure 5f, hiss diffusion is effective over all pitch angle for energies $\gtrsim$500 keV and the VLF transmitter waves are insufficiently strong to contribute. At lower energies the VLF transmitter waves do contribute, however, either through filling the minima in $D_{\alpha\alpha}$ or by providing scattering at low pitch angles.

One of the largest open questions concerning VLF transmitter waves in the radiation belts is whether or not the waves are ducted by density enhancements (Clilverd et al., 2008; Gamble et al., 2008; Sauvaud et al., 2008; Zhang et al., 2018). In this paper we follow Ma et al. (2017) in our assumptions on the ducted to nonducted wave power ratio. These assumptions are based on observed reductions in wave power above the half electron gyrofrequency (Clilverd et al., 2008; Ma et al., 2017) and ray tracing simulations (Clilverd & Horne, 1996); however, the ratios are still uncertain, and hence, we also consider the extreme cases of ducted and nonducted alone. We show that loss time scales are fairly insensitive to this ratio, except for low energies $E \lesssim$100 keV. From a forecasting and global modeling view point, it is partly reassuring that the assumption on the ducted to nonducted ratio does not strongly effect electron lifetimes.

Comparisons of electron decay time scale with observations in the inner belt are problematic. First, observations of high-energy electron fluxes are infrequent (Claudepierre et al., 2017). Second, the long decay time scales, $\gtrsim$1,000 days, make a like-for-like comparison difficult as the inner belt is unlikely to have reached a steady decaying profile before another disturbance occurs. For instance, the time scales calculated from loss cone DEMETER/IDP observations (Benck et al., 2010) likely capture temporary low pitch angle losses rather than whole distribution decay. The electron lifetimes presented here correspond to the lowest eigenvalues of pitch angle diffusion models (Lyons & Thorne, 1973), which can differ significantly from the higher eigenvalues, which contribute on shorter times, complicating the interpretation of observations of electron flux decay (Albert & Shprits, 2009; Baker et al., 2007).

8. Conclusions

We have calculated MLT- and longitude-dependent electron equatorial pitch angle diffusion coefficients between $L = 1.1$ and 3.0, for each ground-based VLF transmitter using Van Allen Probes measurements. These coefficients have then been incorporated into a 1-D pitch angle diffusion model with implicit MLT and longitude dependence to explore the effect of VLF transmitter waves. Our main results are as follows:

1. Despite the localized nature of the VLF transmitter waves, we find that global averages of the wave power, determined by averaging the wave power over MLT and longitude, capture the long-term dynamics of the loss process.
2. At subrelativistic energies, $E \sim$ 40 keV, VLF transmitter waves reduce electron lifetimes by an order of magnitude or more, down to the order of 100 days, in the bulk of the slot region.
3. At moderate relativistic energies, $E \sim$ 500 keV, VLF transmitter waves reduce electron lifetimes by an order of magnitude or more, down to the order of 200 days near the outer edge of the inner radiation belt.
4. VLF transmitter waves are ineffective at removing multi–megaelectron volt electrons from the inner belt and slot region. Our work suggests that they are not responsible for the so-called impenetrable barrier.
5. In general, nonducted VLF transmitter waves are marginally less effective than ducted VLF transmitter waves at reducing electron lifetimes by a factor of 1–4.

The VLF transmitter diffusion coefficients constructed here will be used in global radiation belt models to help improve understanding of the long-term behavior of the inner radiation belt and slot region.

Appendix A: Poynting Flux

Following Albert (2012), we define

$$\rho_1 = \left(1 - \hat{S}\right) \sin\psi \cos\psi / \left[\hat{D}\left(\sin^2\psi - \hat{P}\right)\right], \tag{A1}$$

$$\rho_2 = \left(1 - \hat{S}\right) / \hat{D}, \tag{A2}$$

$$\rho_{m2} = \hat{D}\left(\hat{P} - \sin^2\psi\right) / \left[\hat{P}\left(1 - \hat{S}\right)\right], \tag{A3}$$

$$\rho_{m1} = \rho_{m2} \tan\psi, \tag{A4}$$

$$X = \hat{P} / \left(\hat{P} - \sin^2\psi\right) \tag{A5}$$

where $(\hat{S}, \hat{D}, \hat{P})$ are defined as $(S, D, P)/\mu^2$ where (S, D, P) are the Stix cold plasma quantities (Stix, 1992). These can then be used to convert the EMFISIS equatorial electric field observations, split into ducted and nonducted, into magnetic field intensities, via

$$\frac{E_w^2}{B_w^2} = \frac{1 + \rho_1^2 + \rho_2^2}{1 + \rho_{m1}^2 + \rho_{m2}^2} \frac{\rho_{m2}^2}{\mu^2 \cos^2 \psi}. \tag{A6}$$

and from this the Poynting flux, for ducted and nonducted, in Gaussian units, can be calculated using

$$S_w = \frac{c}{4\pi} \frac{\left[\left(\tan\psi - \rho_1\rho_2 X\right)^2 + \left(1 + \rho_2^2 X\right)^2\right]^{1/2}}{\rho_2^2 X^2 \mu \cos\psi \left(1 + \rho_{m1}^2 + \rho_{m2}^2\right)} B_w^2. \tag{A7}$$

Acknowledgments
We are grateful for the Van Allen Probes data from the EMFISIS instrument obtained from the website (https://emsis.physics.uiowa.edu/data/index). The research leading to these results has received funding from the National Environment Research Council Highlight Topic Grant NE/P10738X/1 (Rad-Sat) and National Environment Research Council Grant NE/R016455/1. The data from the figures are available at the website (https://doi.org/10.5285/93ff55bf-7415-44c8-8e3d-7e2f5c5ffd6d).

References

Abel, B., & Thorne, R. M. (1998). Electron scattering loss in Earth's inner magnetosphere: 2. Sensitivity to model parameters. *Journal of Geophysical Research*, *103*(A2), 2397–2407.

Agapitov, O. V., Artemyev, A. V., Mourenas, D., Kasahara, Y., & Krasnoselskikh, V. (2014). Inner belt and slot region electron lifetimes and energization rates based on AKEBONO statistics of whistler waves. *Journal of Geophysical Research: Space Physics*, *119*, 2876–2893. https://doi.org/10.1002/2014JA019886

Albert, J. M. (2008). Efficient approximations of quasi-linear diffusion coefficients in the radiation belts. *Journal of Geophysical Research*, *113*, A06208. https://doi.org/10.1029/2007JA012936

Albert, J. M. (2012). Dependence of quasi-linear diffusion coefficients on wave parameters. *Journal of Geophysical Research*, *117*, A09224. https://doi.org/10.1029/2012JA017718

Albert, J. M., & Shprits, Y. Y. (2009). Estimates of lifetimes against pitch angle diffusion. *Journal of Atmospheric and Solar-Terrestrial Physics*, *71*(16), 1647–1652.

Albert, J. M., Starks, M. J., Horne, R. B., Meredith, N. P., & Glauert, S. A. (2016). Quasi-linear simulations of inner radiation belt electron pitch angle and energy distributions. *Geophysical Research Letters*, *43*, 2381–2388. https://doi.org/10.1002/2016GL067938

Baker, D. N., Kanekal, S. G., Horne, R. B., Meredith, N. P., & Glauert, S. A. (2007). Low-altitude measurements of 2–6 MeV electron trapping lifetimes at 1.5 L2.5. *Geophysical Research Letters*, *34*, L20110. https://doi.org/10.1029/2007GL031007

Benck, S., Mazzino, L., Cyamukungu, M., Cabrera, J., & Pierrard, V. (2010). Low altitude energetic electron lifetimes after enhanced magnetic activity as deduced from SAC-C and DEMETER data. *Annales Geophysicae*, *28*(3), 849–859.

Brautigam, D. H., & Albert, J. M. (2000). Radial diffusion analysis of outer radiation belt electrons during the October 9, 1990, magnetic storm. *Journal of Geophysical Research*, *105*(A1), 291–309.

Claudepierre, S. G., O'Brien, T. P., Fennell, J. F., Blake, J. B., Clemmons, J. H., Looper, M. D., et al. (2017). The hidden dynamics of relativistic electrons (0.7–1.5 MeV) in the inner zone and slot region. *Journal of Geophysical Research: Space Physics*, *122*, 3127–3144. https://doi.org/10.1002/2016JA023719

Clilverd, M. A., & Horne, R. B. (1996). Ground-based evidence of latitude-dependent cyclotron absorption of whistler mode signals originating from VLF transmitters. *Journal of Geophysical Research*, *101*(A2), 2355–2367.

Clilverd, M. A., Rodger, C. J., Gamble, R., Meredith, N. P., Parrot, M., Berthelier, J. J., & Thomson, N. R. (2008). Ground-based transmitter signals observed from space: Ducted or nonducted? *Journal of Geophysical Research*, *113*, A04211. https://doi.org/10.1029/2007JA012602

Cohen, M. B., Inan, U. S., & Paschal, E. W. (2010). Sensitive broadband ELF/VLF radio reception with the AWESOME instrument. *IEEE Transactions on Geoscience and Remote Sensing*, *48*(1), 3–17.

Foster, J. C., Erickson, P. J., Baker, D. N., Jaynes, A. N., Mishin, E. V., Fennel, J. F., et al. (2016). Observations of the impenetrable barrier, the plasmapause, and the VLF bubble during the 17 March 2015 storm. *Journal of Geophysical Research: Space Physics*, *121*, 5537–5548. https://doi.org/10.1002/2016JA022509

Gallagher, D. L., & Craven, P. D. (2000). Global core plasma model based on observations, have been developed for various analytical representation that is continuous in value and The work by Persoon et is now often used The GCPM is intended to take advantage of existing models, In the plasmasp. *Journal of Geophysical Research*, *105*(A8), 18,819–18,833.

Gamble, R. J., Rodger, C. J., Clilverd, M. A., Sauvaud, J. A., Thomson, N. R., Stewart, S. L., et al. (2008). Radiation belt electron precipitation by man-made VLF transmissions. *Journal of Geophysical Research*, *113*, A10211. https://doi.org/10.1029/2008JA013369

Glauert, S. A., & Horne, R. B. (2005). Calculation of pitch angle and energy diffusion coefficients with the PADIE code. *Journal of Geophysical Research*, *110*, A04206. https://doi.org/10.1029/2004JA010851

Helliwell, R. A. (1965). *Whistlers and related ionospheric phenomena*. Stanford, CA: Stanford University Press.

Horne, R. B., Kersten, T., Glauert, S. A., Meredith, N. P., Boscher, D., Sicard-Piet, A., et al. (2013). A new diffusion matrix for whistler mode chorus waves. *Journal of Geophysical Research: Space Physics*, *118*, 6302–6318. https://doi.org/10.1002/jgra.50594

Inan, U. S., Chang, H. C., & Helliwell, R. A. (1984). Electron precipitation zones around major ground-based VLF signal sources. *Journal of Geophysical Research*, *89*(A5), 2891–2906.

Karpman, V. I., & Kaufman, R. N. (1982). Whistler wave propagation in density ducts. *Journal of Plasma Physics*, *27*, 225–238.

Kennel, C. F. (1969). Consequences of a magnetospheric plasma. *Reviews of Geophysics*, *7*(1-2), 379–419.

Kulkarni, P., Inan, U. S., Bell, T. F., & Bortnik, J. (2008). Precipitation signatures of ground-based VLF transmitters. *Journal of Geophysical Research*, *113*, A07214. https://doi.org/10.1029/2007JA012569

Li, X., Selesnick, R. S., Baker, D. N., Jaynes, A. N., Kanekal, S. G., Schiller, Q., et al. (2015). Upper limit on the inner radiation belt MeV electron intensity. *Journal of Geophysical Research: Space Physics*, *120*, 1215–1228. https://doi.org/10.1002/2014JA020777

Looper, M. D., Blake, J. B., & Mewaldt, R. A. (2005). Response of the inner radiation belt to the violent Sun-Earth connection events of October-November 2003. *Geophysical Research Letters*, *32*, L03S06. https://doi.org/10.1029/2004GL021502

Lyons, L. R., & Thorne, R. M. (1973). Equilibrium structure of radiation belt electrons. *Journal of Geophysical Research*, *78*(13), 2142–2149.

Lyons, L. R., Thorne, R. M., & Kennel, C. F. (1972). Pitch-angle diffusion of radiation belt electrons within the plasmasphere. *Journal of Geophysical Research*, *77*(19), 3455–3474.

Ma, Q., Mourenas, D., Li, W., Artemyev, A., & Thorne, R. M. (2017). VLF waves from ground-based transmitters observed by the Van Allen Probes: Statistical model and effects on plasmaspheric electrons. *Geophysical Research Letters*, *44*, 6483–6491. https://doi.org/10.1002/2017GL073885

Meredith, N. P., Horne, R. B., Clilverd, M. A., Horsfall, D., Thorne, R. M., & Anderson, R. R. (2006). Origins of plasmaspheric hiss. *Journal of Geophysical Research*, *111*, A09217. https://doi.org/10.1029/2006JA011707

Meredith, N. P., Horne, R. B., Clilverd, M. A., & Ross, J. P. J. (2019). An investigation of VLF transmitter wave power in the inner radiation belt and slot region. *Journal of Geophysical Research: Space Physics*, *124*. https://doi.org/10.1029/2019JA026715

Meredith, N. P., Horne, R. B., Glauert, S. A., & Anderson, R. R. (2007). Slot region electron loss timescales due to plasmaspheric hiss and lightning-generated whistlers. *Journal of Geophysical Research*, *112*, 1–12. https://doi.org/10.1029/2007JA012413

Meredith, N. P., Horne, R. B., Kersten, T., Li, W., Bortnik, J., Sicard, A., & Yearby, K. H. (2018). Global model of plasmaspheric hiss from multiple satellite observations. *Journal of Geophysical Research: Space Physics*, *123*, 4526–4541. https://doi.org/10.1029/2018JA025226

Mourenas, D., Artemyev, A. V., Ripoll, J. F., Agapitov, O. V., & Krasnoselskikh, V. V. (2012). Timescales for electron quasi-linear diffusion by parallel and oblique lower-band chorus waves. *Journal of Geophysical Research*, *117*, A06234. https://doi.org/10.1029/2012JA017717

Ozhogin, P., Tu, J., Song, P., & Reinisch, B. W. (2012). Field-aligned distribution of the plasmaspheric electron density: An empirical model derived from the IMAGE RPI measurements. *Journal of Geophysical Research*, *117*, A06225. https://doi.org/10.1029/2011JA017330

Picone, J. M., Hedin, A. E., Drob, D. P., & Aikin, A. C. (2002). NRLMSISE-00 empirical model of the atmosphere: Statistical comparisons and scientific issues. *Journal of Geophysical Research*, *107*(A12), 1468. https://doi.org/10.1029/2002JA009430

Ripoll, J. F., Albert, J. M., & Cunningham, G. S. (2014). Electron lifetimes from narrowband wave-particle interactions within the plasmasphere. *Journal of Geophysical Research: Space Physics*, *119*, 8858–8880. https://doi.org/10.1002/2014JA020217

Rosen, A., & Sanders, N. L. (1971). Loss and replenishment of electrons in the inner radiation zone during 1965–1967. *Journal of Geophysical Research*, *76*, 110.

Sauvaud, J. A., Maggiolo, R., Jacquey, C., Parrot, M., Berthelier, J. J., Gamble, R. J., & Rodger, C. J. (2008). Radiation belt electron precipitation due to VLF transmitters: Satellite observations. *Geophysical Research Letters*, *35*, L09101. https://doi.org/10.1029/2008GL033194

Selesnick, R. S. (2012). Atmospheric scattering and decay of inner radiation belt electrons. *Journal of Geophysical Research*, *117*, A08218. https://doi.org/10.1029/2012JA017793

Selesnick, R. S., Albert, J. M., & Starks, M. J. (2013). Influence of a ground-based VLF radio transmitter on the inner electron radiation belt. *Journal of Geophysical Research: Space Physics*, *118*, 628–635. https://doi.org/10.1002/jgra.50095

Selesnick, R. S., Su, Y. J., & Blake, J. B. (2016). Control of the innermost electron radiation belt by large-scale electric fields. *Journal of Geophysical Research: Space Physics*, *121*, 8417–8427. https://doi.org/10.1002/2016JA022973

Shi, R., Summers, D., Ni, B., Fennell, J. F., Blake, J. B., Spence, H. E., & Reeves, G. D. (2016). Survey of radiation belt energetic electron pitch angle distributions based on the Van Allen Probes MagEIS measurements. *Journal of Geophysical Research: Space Physics*, *121*, 1078–1090. https://doi.org/10.1002/2015JA021724

Spjeldvik, W. N., & Rothwell, P. L. (1985). The radiation belts.

Spjeldvik, W. N., & Thorne, R. M. (1975). The cause of storm after effects in the middle latitude D-region. *Journal of Atmospheric and Terrestrial Physics*, *37*(5), 777–795.

Starks, M. J., Quinn, R. A., Ginet, G. P., Albert, J. M., Sales, G. S., Reinisch, B. W., & Song, P. (2008). Illumination of the plasmasphere by terrestrial very low frequency transmitters: Model validation. *Journal of Geophysical Research*, *113*, A09320. https://doi.org/10.1029/2008JA013112

Stix, T. H. (1992). *Waves in plasmas*. New York: American Institute of Physics.

Su, Y.-J., Selesnick, R. S., & Blake, J. B. (2016). Formation of the inner electron radiation belt by enhanced large-scale electric fields. *Journal of Geophysical Research: Space Physics*, *121*, 8508–8522. https://doi.org/10.1002/2016JA022881

Summers, D., & Thorne, R. M. (2003). Relativistic electron pitch-angle scattering by electromagnetic ion cyclotron waves during geomagnetic storm. *Journal of Geophysical Research*, *108*(A4), 1143. https://doi.org/10.1029/2002JA009489

Tao, X., Bortnik, J., & Friedrich, M. (2010). Variance of transionospheric VLF wave power absorption. *Journal of Geophysical Research*, *115*, A07303. https://doi.org/10.1029/2009JA015115

Vette, J. I. (1991). The AE-8 trapped electron model environment (*92*). Greenbelt, MD: NASA STI/Recon Technical Report N.

Walt, M., & Farley, T. A. (1976). The physical mechanisms of the inner Van Allen belt. *Fundamentals of Cosmic Physics*, *2*, 1–110.

Walt, M., & MacDonald, W. M. (1964). The influence of the Earth's atmosphere on geomagnetically trapped particles. *Reviews of Geophysics and Space Physics*, *2*, 543–577.

Zhang, Z., Chen, L., Li, X., Xia, Z., Heelis, R. A., & Horne, R. B. (2018). Observed propagation route of VLF transmitter signals in the magnetosphere. *Journal of Geophysical Research: Space Physics*, *123*, 5528–5537. https://doi.org/10.1029/2018JA025637